



### Science Arts & Métiers (SAM)

is an open access repository that collects the work of Arts et Métiers Institute of Technology researchers and makes it freely available over the web where possible.

This is an author-deposited version published in: <https://sam.ensam.eu>  
Handle ID: <http://hdl.handle.net/10985/6895>

#### To cite this version :

Guy CAIGNAERT, Gérard BOIS, Jean-Baptiste LEROUX, Olivier COUTIER-DELGOSHA -  
Influence of the Blade Number on Inducer Cavitating Behavior - Journal of Fluids Engineering -  
Vol. 134, p.11 - 2012

Any correspondence concerning this service should be sent to the repository

Administrator : [scienceouverte@ensam.eu](mailto:scienceouverte@ensam.eu)



**O. Coutier-Delgosha**  
e-mail: olivier.coutier@ensam.eu

**G. Caignaert**  
e-mail: guy.caignaert@ensam.eu

**G. Bois**  
e-mail: gerard.bois@ensam.eu

**J.-B. Leroux<sup>1</sup>**  
e-mail: jean-baptiste.leroux@ensieta.fr

Arts et Metiers ParisTech/LML Laboratory,  
8 Boulevard Louis XIV,  
59046 Lille Cedex, France

# Influence of the Blade Number on Inducer Cavitating Behavior

*Effects of the blade number on the performance of a rocket engine turbopump inducer are investigated in the present paper. For that purpose, two inducers characterized by three blades and five blades, respectively, were manufactured and tested experimentally. The two inducers were designed on the basis of identical design flow rate and identical pressure elevation at nominal flow rate. The first part of the study focuses on the steady behavior of the inducers in cavitating conditions: evolutions of performance, torque, mass flow rate, and amplitude of radial forces on the shaft according to the inlet pressure are considered. Several flow rates and rotation speeds are investigated. Significant differences between the inducers are obtained concerning the critical cavitation number, the amplitude of the radial forces, and the organization of cavitation in the machinery. Cavitation instabilities are investigated in the second part of the study. Various flow patterns are detected according to the mass flow rate and the cavitation number. [DOI: 10.1115/1.4006693]*

## 1 Introduction

To achieve high rotation speed and low suction pressure, rocket engine turbopumps are usually equipped with a first stage called inducer. This axial runner (Fig. 1), which operates in cavitating conditions, should elevate the pressure sufficiently so that the next centrifugal impellers can operate without any perturbation due to cavitation. So maintaining its nominal performance in cavitating conditions is necessary to ensure the correct functioning of the whole turbopump.

However, performance of rocket engine turbopump inducers is greatly influenced by the development of cavitation in the flow. Sheet cavitation and tip cavitation, when they increase, progressively degrade the inducer performance and also induce significant radial and axial efforts on the shaft, which may as well compromise the rotor equilibrium as lead to problematic pressure fluctuations at the inducer outlet.

Moreover, significant unsteady effects are usually detected when the vapor volume becomes significant in the machinery. Experimental results point out two main types of cavitation instabilities: a self-oscillation behavior of cavitation sheets, whose mechanism was studied in cavitation tunnels and analyzed by many authors (including Kubota et al. [1] and Le et al. [2]), and a coupling between the cavitation areas in the different blade to blade channels. This second type of instability consists for example of different sizes of sheet cavities on the blades. Such dissymmetry can also be steady in the inducer rotating frame or unsteady, leading in this case to the so-called super or subsynchronous rotating cavitation, whether the dissymmetry rotates faster or slower than the inducer.

This last phenomenon strongly depends on the cavitation development in the machine. A typical sketch in the case of a four blade inducer is given for example on Fig. 2 [3]: at cavitation inception, only a steady and balanced flow pattern with one short attached cavity on each blade is observed from flow visualizations. When cavitation parameter is slightly decreased, a steady and alternate cavitating configuration appears with alternatively one short and one long cavity. For a lower cavitation parameter, just above breakdown, an unsteady flow pattern called rotating cavitation can be identified [4,5]. Unbalanced attached cavities are observed in the different channels, their distribution rotating faster than the

inducer and leading to large radials loads on the shaft. Finally, near the breakdown of the inducer, a steady and balanced flow pattern with fully developed cavitation is observed. Some attempts to explain inception and mechanisms of rotating cavitation have been proposed in previous studies [6,7]. Yoshida and colleagues state that inception of unstable behaviors is mainly governed by the sheet cavity length. Sheet cavities longer than the cascade throat remain equal because they are fully constrained by the adjacent blade. Conversely, sheet cavities that do not reach the cascade throat ( $0.8 < L_c/h < 1$ ) are characterized by a degree of freedom, which may lead to unstable cavitation such as synchronous nonsymmetrical flow patterns.

However, no consensus is presently obtained concerning as well the mechanisms that are responsible for the inception of unbalanced flow patterns as the ones that control the successive synchronous and nonsynchronous regimes that are usually observed in inducers.

In practice, these instabilities must be quantified and controlled to avoid any major effect on the global pump behavior. For that purpose, several parameters of the inducer design, such as the shape of the blade leading edge, the hub shape, or the spacing of the blades, have been varied in previous studies. The recurrent objective of these studies is to optimize the cavitating behavior, especially by suppressing rotating cavitation patterns.

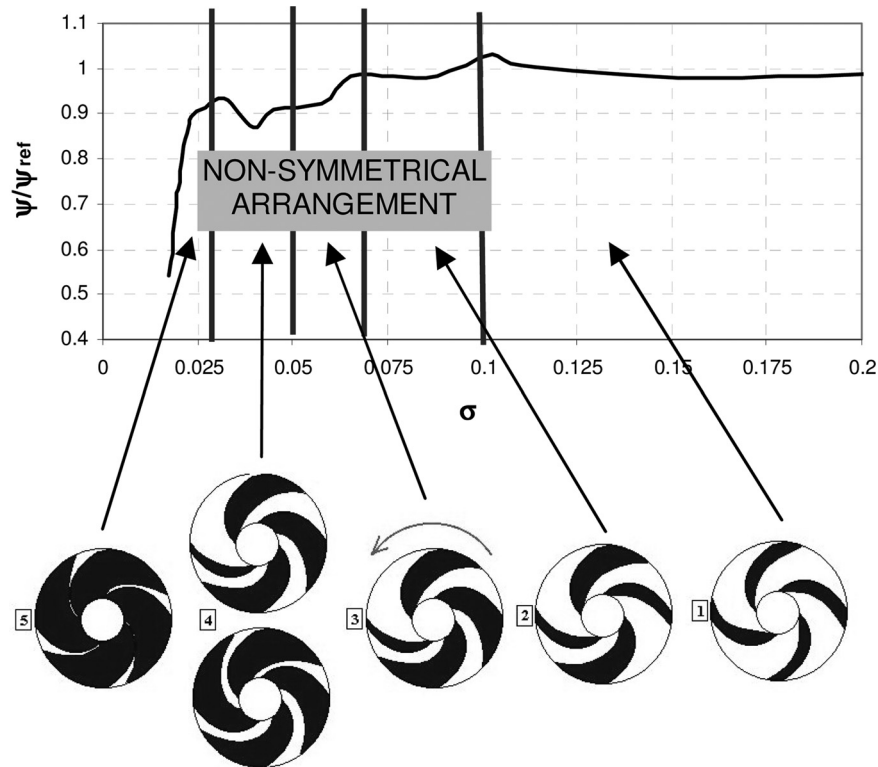
Concerning the influence of the blade leading edge shape, Bakir et al. [8] have shown that increasing the slope of the leading edge (in a front view) leads to significant improvement of the inducer



Fig. 1 Rocket engine turbopump inducer

<sup>1</sup>Present address: ENSIETA - Laboratoire MSN, 2 Rue François Verny, 29806 Brest Cedex 9, France.

Contributed by the Fluids Engineering Division of ASME for publication in the JOURNAL OF FLUIDS ENGINEERING. Manuscript received February 26, 2010; final manuscript received August 26, 2011; published online August 9, 2012. Assoc. Editor: Theodore J. Heindel.



**Fig. 2 Sketches of cavitation patterns and performance evolution as the cavitation number decreases in a four-blade inducer (from Jousselein et al. [3])**

cavitating performance at high flow rate (reduction of the critical cavitation number) and also to a decrease of the amplitude of the pressure fluctuations. This result was also obtained by Yoshida et al. [9] who found that rotation cavitation could be reduced by enhancing alternate blade cavitation with alternate cut-back of the blade leading edges.

The effects of unequal spacing of the blades have been investigated by Horiguchi et al. [10] by numerical simulations. It has been found that unequally spacing the blade spacing decreases the cavitation number corresponding to inception of rotating cavitation. It also slightly increases the frequency of cavitation surge.

Conversely, a limited number of studies can be found concerning the influence of the blade number. According to Japikse [11], the design practice concerning this point is usually based on conventional experience: inducers usually have been manufactured with one to four blades in the inlet section. Problems of instability may appear in all cases, because of possible cavitation on a single blade, but not on the other(s). However, this author states that three-bladed inducers may have fewer dynamic stability problems than two-bladed and four-bladed ones, since alternate cavitation is avoided.

The objective of the present study is to make clearer the effects of the blade number on the behavior of a rocket engine turbopump inducer. Attention is focused on three blade and five blade inducers because only a few studies have been devoted to their cavitating behavior until now. For that purpose, two inducers with three blades and five blades, respectively, have been designed and manufactured. Their design flow rate is identical as well as the pressure elevation at nominal flow rate. Moreover, the design process is also the same. The two inducers have been tested experimentally by varying the inlet pressure, the flow rate, and the rotation speed, so various cavitating behaviors have been investigated.

The present paper focuses on the evolution of the inducer cavitating behavior when the inlet pressure is decreased. Evolutions of performance, torque, efficiency, and amplitude of radial and axial forces on the shaft according to the inlet pressure are considered. Detection of unsteady cavitation patterns, on the basis of radial

forces measurements, is also included. The objective is to compare the results obtained with the two inducer geometries in order to determine the influence of the blade number on quasi-steady and unsteady features of the inducer behavior. Note that all results presented in the paper are dimensionless for reasons of confidentiality. So, the superscript “+” indicates that each variable  $V^+$  is  $V/V_0$  where  $V_0$  is a reference value, which is not given.

## 2 Experimental Setup

**2.1 Inducer Geometries.** Two inducers were designed and manufactured by SNECMA Moteurs according to the same design rules, with three and five blades, respectively. They will be denoted IND3 and IND5, respectively, hereafter. For confidentiality reasons, only qualitative differences between the two inducers are given here. The axial length is identical for both inducers, so solidity is higher for IND5 than for IND3. The blade angles at the leading edge are nearly the same, so the flow incidence at the leading edge is not modified between IND3 and IND5. Conversely, the angles at the trailing edge are slightly modified to keep the same hydraulic performance.

**2.2 Test Facility.** The LML laboratory large test facility devoted to the study of axial pumps in cavitating conditions has been used for the experiments. This two-stairs facility is equipped with a 200 kW motor that is able to reach an inducer rotation speed of 6000 rpm. The device upstairs (Fig. 3) is mainly composed of the inducer to be tested and a stator downstream from the inducer that conducts the flow towards the discharge pipe. The inlet and discharge pipes are connected to two tanks. A free surface is maintained in the upstream one so that the pressure can be controlled in the installation, from about 0.1 bars up to 16 bars. A part  $Q_s$  of the mass flow rate is taken at the inducer outlet for the axial equilibrium device and then reinjected in the upstream tank. Downstairs are located two large resorption tanks used for the extraction of dissolved gas, a variable head loss device that

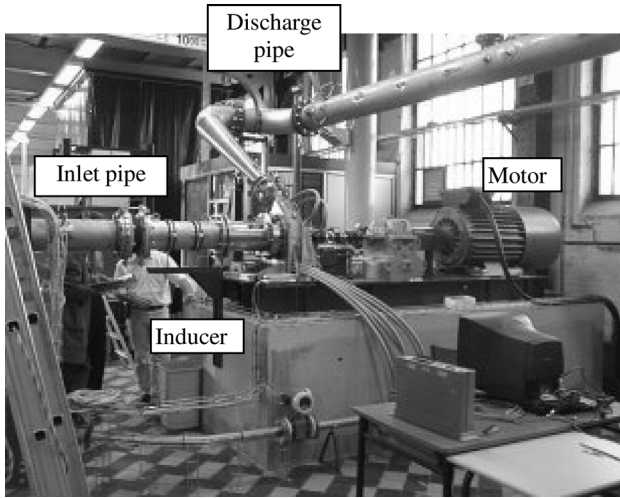


Fig. 3 General view of the LML large test facility

enables the control of the flow rate, and the vacuum pump used to decrease the pressure in the inlet tank. A heat exchanger is also connected to the facility to control the water temperature.

**2.3 Acquisition Device.** The inducer test section is equipped with a large variety of sensors devoted either to the characterization of steady flow properties or to the analysis of the flow unsteady fluctuations.

Concerning steady flow properties, the torque  $M_x$  and the rotation speed  $N$  are measured with a Torquemaster TM213 torque meter, while a Rosemount AP6 pressure transducer (range 0–6 bars) is used for the inlet pressure  $P_i$ . A Rosemount DP7E22 differential pressure transducer (range 0–16 bars) connected between  $P_i$  and  $P_d$  is used to directly obtain the elevation  $\Delta P$ . The main flow rate  $Q_m$  and the recirculating one  $Q_s$  are measured with Endress + Hauser electromagnetic flow meters. The motor shaft rotation speed is also controlled with a photoelectric cell.

Temperature measurements are performed on the upstream and downstream bearings of the inducer shaft to control their increase

at high rotation speed, and the water temperature is measured to regulate the heat exchanger operation so that a 25 °C temperature is maintained in the flow.

Moreover, fourteen pressure taps located on the inducer casing are connected to a Endress + Hauser pressure sensor (range 0–6 bars), and the 14 taps are successively connected during 10 s to the sensor, with the use of electrovalves (only the last 5 s are recorded for each tap, in order to eliminate transient effects due to the changeover of the taps).

The torque  $M_x$  and the rotation speed  $\omega$  are acquired at frequency 100 Hz during 10 s, while all other signals are recorded at frequency 40 Hz during 140 s. From these records, mean and RMS values of the signals are calculated for each investigated flow condition.

Note that the inlet and outlet pressures are measured in the inlet and delivery pipes more than 1 m upstream and downstream from the inducer, so the calculated pressure head includes the head losses between the two pressure taps, including the one in the stator and in the downstream 90 deg bends that can be seen in Fig. 4.

Absolute uncertainties on the mean flow characteristics are 0.5% of  $Q_{ref}$  for  $Q_m$ , 0.05% of  $Q_{ref}$  for  $Q_s$ , 0.25% of  $N_{ref}$  for  $N$ , 2% of the noncavitating torque value for  $M_x$ , and 0.2% of the measurement range for the upstream pressure and  $\Delta P$ . Precision regarding the cavitation number and the head, torque, and flow rate coefficients depend on the flow conditions and will be indicated in the figures hereafter.

Unsteady flow properties are investigated with nine Kistler 701A piezoelectric pressure transducers (Fig. 4): six of them are located in the upstream and delivery pipes, two other ones ( $P'_1$  and  $P'_2$ ) are located at the inlet of the inducer test section, and the last one  $P'_3$  is between the inducer and the stator. All transducers are mounted flush to the internal pipe wall. Four accelerometers are also installed on the inducer casing to measure the vibrations in the axial and radial directions. A six components balance is mounted on the shaft to obtain the axial force  $F_x$ , the radial forces  $F_y$  and  $F_z$ , the torque  $M_x$ , and also the bending moments  $M_y$  and  $M_z$ . Six bridges of strain gauges are located on the inducer shaft, in three different cross sections. Piezoresistive gauges are used. The frequency response of this device has been validated in the range 0–30 Hz, which includes the present range of investigations (frequency of instabilities in the rotating frame).

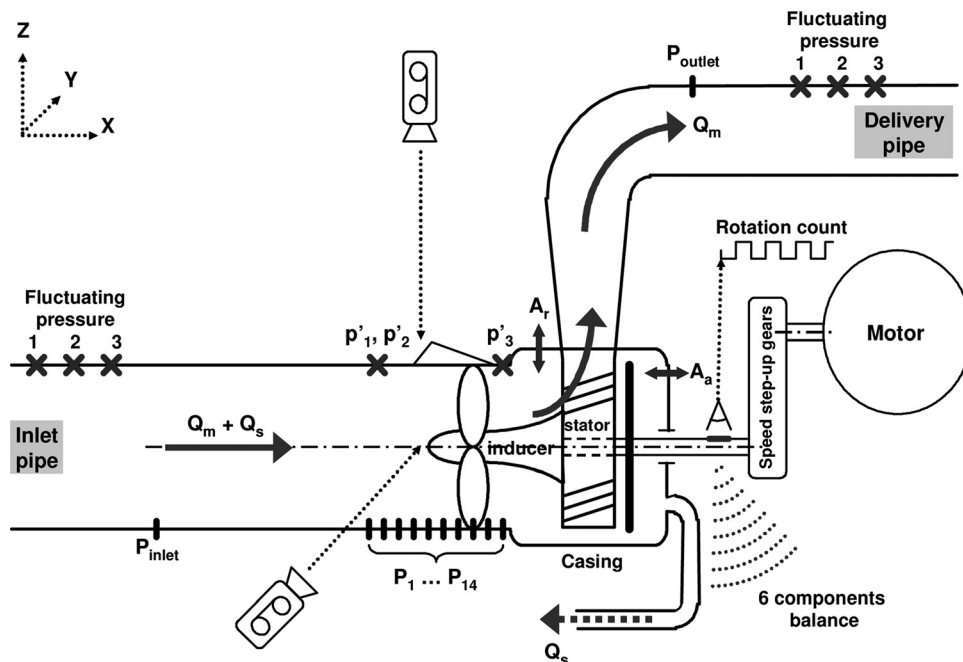


Fig. 4 Scheme of the inducer test section including the acquisition equipment

The 19 unsteady parameters are recorded simultaneously at frequency 2048 Hz with the LMS CADA-X code. An antialiasing filtering (Butterworth, 800 Hz, -50 dB/octave) is applied during acquisition.

Relative uncertainty on the pressure and vibration measurements is found to be close to 1% in noncavitating conditions and 2% in cavitating conditions. Precision on the forces and moments measured by the balance is estimated to 1% of the measurement ranges.

**2.4 Visualizations.** Visualizations are performed with a special Plexiglas casing that imposes a maximal rotation speed of  $0.6 N_{ref}$  in order to avoid erosion. Two digital Marlin cameras are used to obtain a front view and a side view of the inducer. Images are recorded every eight rotations, which corresponds to a frequency close to 6.25 Hz. The camera resolution is  $640 \times 480$ . Image records are performed simultaneously with transducer acquisitions so that the correspondence between the pictures and all the recorded parameters can be obtained.

**2.5 Experimental Process.** Two types of experiments were performed:

- Type #1: Steady state flow configurations are investigated by setting the flow rate and rotation speed and then recording the 20 parameters listed previously. The inlet pressure is decreased by successive steps, from 2 bars (noncavitating behavior) down to the pressure that corresponds to a 25% drop of the inducer head. Note that during this process, the variable head loss device is used to decrease the head loss in the facility in order to maintain a constant flow rate even for severe cavitating conditions.
- Type #2: Unsteady flow properties are investigated by varying continuously the inlet pressure from 2 bars down to the 25% drop of the inducer head. The duration of the pressure decrease is about 360 s, which may result in quasi-steady flow conditions (this point is checked in Sec. 2). During this process, the variable head loss device position is not modified, so the mass flow rate progressively decreases together with the inducer elevation.

### 3 Mean Flow Properties

**3.1 Comparison Between Type #1 and Type #2 Processes.** Mean flow properties were investigated both by type #1 and type #2 experiments. To compare the results, head drop and torque drop charts obtained with IND3 at rotation speed  $N = N_{ref}$  and flow rate  $Q = Q_n$  are drawn in Figs. 5(a) and 5(b). In both images, the measurements resulting from steady flow conditions and from continuous pressure decrease are presented. Two sets of data recorded at different times are reported for type #2 experiments in order to estimate the repeatability of the measurements. Note also that the uncertainties regarding  $\tau^+$ ,  $\psi^+$ , and  $\chi^+$  are indicated on the charts. A close agreement between the two types of experiments is obtained concerning the  $\psi^+$  evolution in low cavitating conditions. Conversely, a slight discrepancy can be observed in the case of  $\chi^+$ . It must be reminded that the torque is obtained from a torquemeter in type #1 experiments, whereas it is derived from the six components balance measurements in type #2 experiments. So the difference, which is systematically lower than the magnitude of the uncertainty, may be mainly due to the use of these two different devices. A significant discrepancy between the two sets of results is also obtained in the  $\tau^+$  scale during the performance drop. This is directly due to the flow rate, which is maintained to its initial value in the type #1 experiment, while it decreases progressively in the type #2 experiment.

It can be noticed also that a significant drop and reincrease of  $\psi^+$  is obtained in type #1 experiments for  $\tau^+$  close to 0.2. This effect is slighter in type #2 experiments. Previous studies (Coutier-Delgosha et al. [6]) have demonstrated the connection

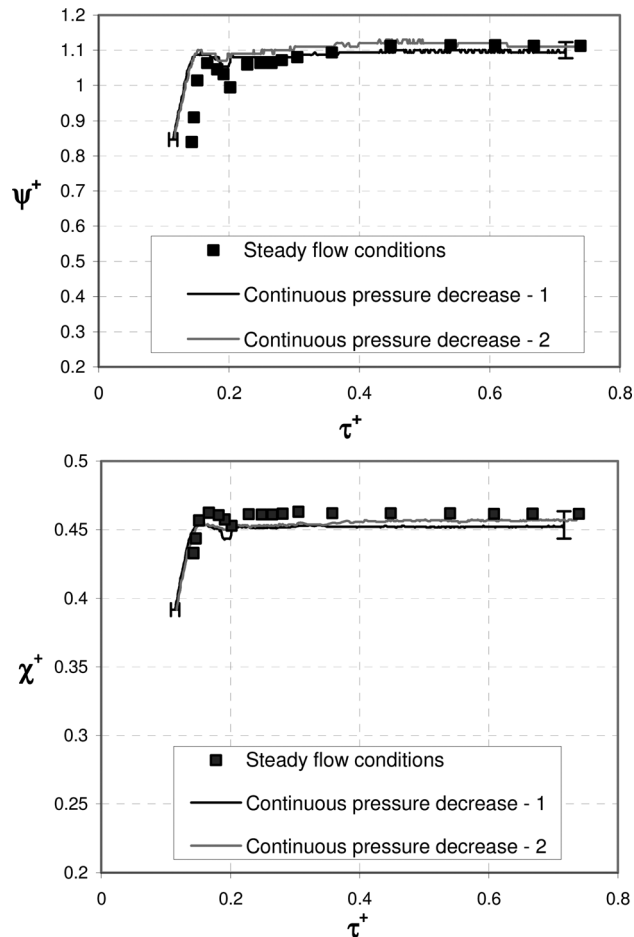


**Fig. 5 (a) Head coefficient drop charts and (b) torque coefficient drop charts (IND3,  $N_{ref}$ ,  $Q_n$ )**

between this moderate drop and the occurrence of unsteady phenomena such as rotating cavitation. So this discrepancy suggests that unsteady flow properties that will be investigated in part 2 of the paper from type #2 experiments may be slightly different from the ones that would be obtained from steady flow experiments.

However, from these results (and similar ones obtained with the other inducer, at other rotation speeds and/or other flow rates), it can be assessed that a fair agreement is generally obtained between both types of experiments, excepted during the final performance drop. It shows that the pressure decrease process is slow enough to obtain quasi-steady flow conditions so transient effects due to continuous flow condition modification can be neglected. This point has been checked with IND3 by slowing down (by a factor 2) the pressure drop for a single mass flow rate at maximum rotation speed and comparing not only the  $\psi^+$  and  $\chi^+$  evolutions, but also the inception, vanishing, and amplitude of instabilities. All differences related to these criteria fall within the range of uncertainty of the measurements.

**3.2 Influence of Rotation Speed.** Still considering IND3, influence of rotation speed on the head coefficient drop chart is investigated in Fig. 6. Note that the measurement uncertainty is the one reported previously in Fig. 5(a). Both type #1 and type #2 experiments are reported. A fair agreement between all results is obtained. All differences of  $\psi$  magnitude remain lower than the uncertainties, while nearly identical charts are obtained during the performance breakdown, as well for type #1 as for type #2 experiments. It suggests that similarity laws may be applied for the three investigated rotation speeds for both types of experiments.

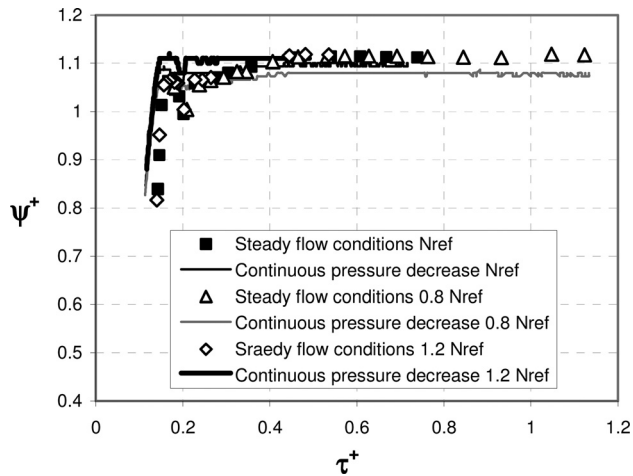


**Fig. 6** Head drop charts for rotation speeds  $N_{ref}$ ,  $0.8 N_{ref}$ , and  $1.2 N_{ref}$  (IND3,  $Q_n$ , type #1 and #2 experiments)

**3.3 Organization of Cavitation.** Visualizations performed during type #2 experiments at rotation speed  $0.6 N_{ref}$  enable us to understand the general mean organization of cavitation inside the inducer when the pressure is progressively decreased. Front views and side views obtained at nominal flow rate for  $\tau^+ = 0.6$  and  $0.25$  are presented in Fig. 7 for both inducers. The first value corresponds to relatively low cavitating conditions, while the second one results in more severe conditions, close to the performance breakdown (see Fig. 5).

The main difference between the two present inducers and previous observations performed in four-blade inducers (Coutier-Delgosha [12]) concerns tip cavitation: this one is much developed in IND3 and IND5 even for low cavitating conditions, whereas it is usually less pronounced in four-blade inducers. From side views, it can be seen also that tip cavitation in IND3 and IND5 develops significantly upstream to the blades, which suggests that it interacts with the inlet shroud recirculation. In all cases, tip cavitation is localized in the azimuthal direction between the leading edge and the cascade throat and, thus, does not occur inside the blade to blade channels.

The reason for such remarkable development of tip cavitation in both inducers is not clear. Indeed, it was expected that IND5 would have much less tip cavitation than IND3 because of the difference of blade load. However, it can be anticipated here that no instability due to cavitation will be found hereafter in Sec. 3.2 for  $\tau^+ = 0.6$ , while in the case of four blade inducers, configurations of alternate

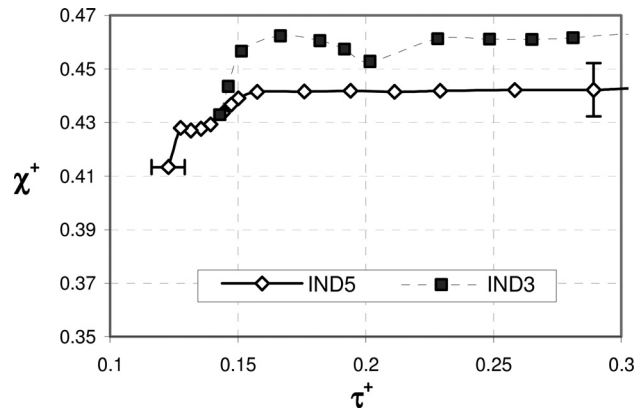


**Fig. 8** Torque coefficient drop for IND3 and IND5 ( $N_{ref}$ ,  $Q_n$ , type #1 experiments)

blade cavitation (nonsymmetrical cavitation pattern with identical vapor development on opposite blades) are usually obtained for such value of the cavitation number. The absence of such asymmetrical stable cavitation pattern in IND3 and IND5 may be connected with the apparent difference of tip cavitation development.

Moreover, development of sheet cavitation seems similar in the two inducers: for  $\tau^+ = 0.6$ , nearly no sheet cavity is observed, while very small ones have appeared at the blade leading edge for  $\tau^+ = 0.25$ . This is consistent with the design process, which did not induce any significant modification of the blade angles at the leading edge from IND3 to IND5.

**3.4 Study of the Breakdown.** This section focuses on the final performance drop. The behaviors of the two inducers are compared for  $\tau^+$  varying between the breakdown inception and 20%  $\psi^+$  drop, i.e., the limit assigned for the experiments.

Figures 8 and 9 present the evolution of  $\chi^+$  at nominal flow rate and rotation speed  $N_{ref}$  from type #1 and type #2 experiments, respectively. Two records are reported for type #2 experiments with IND3.

It can be noticed first from type #1 experiments that IND3 is characterized before the breakdown by a higher torque coefficient value than IND5 (0.44 for IND5 against 0.46 for IND3). The value assigned for the design of the two inducers was 0.41. Although the measurement uncertainties may be partially responsible for this difference (see the figures), it is clear that the design process has not been permitted to fulfill the exact condition that was required. However, the maximum difference in noncavitating

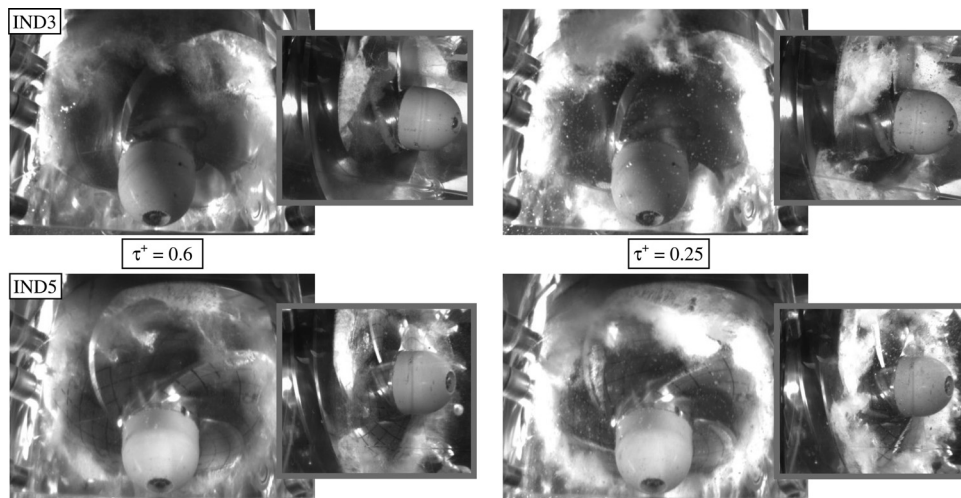


**Fig. 7** Flow visualizations for (a)  $\tau^+ = 0.6$  and (b)  $\tau^+ = 0.25$  ( $0.6 N_{ref}$ ,  $Q_n$ )

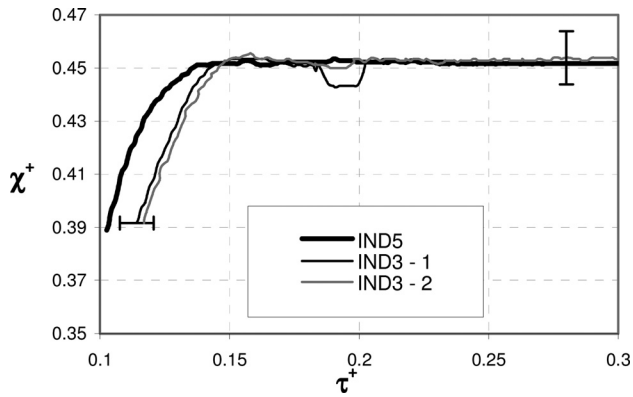


Fig. 9 Torque coefficient drop for IND3 and IND5 ( $N_{ref}$ ,  $Q_n$ , type #2 experiments)

conditions between the two inducers, considering all the tests, is estimated to 5%. This difference, although it may have some minor effects on the results, is sufficiently small to consider that the initial design requirement—identical performance for the two inducers—is verified.

From Figs. 9 and 10, it is clear that inception of breakdown does not occur simultaneously for the two inducers: for both types of experiments, IND3 performance first drops before IND5. Note that the drops obtained with type #1 experiments all occur later than the ones detected by type #2 experiments because the flow rate decreases in this second case (Fig. 10) results during the beginning of the breakdown in an increase of the inducer performance that counterbalances more or less the drop.

To compare more precisely the occurrence of the breakdown for the two inducers, the value of  $\tau_c^+$  corresponding to 3%  $\psi^+$  drop and 3%  $\chi^+$  drop, respectively, is presented in Fig. 11 for rotation speeds varying between  $0.6 N_{ref}$  and  $1.2 N_{ref}$  at nominal flow rate. Results are obtained here from type #2 experiments.

It can be observed that values of  $\tau_c^+$  are systematically higher for the 3%  $\psi^+$  drop than for the 3%  $\chi^+$  drop, which implies that only the losses in the pump increase at the beginning of the breakdown, while the blade load is not affected. Pictures presented in Figs. 12(a) and 12(b) show the cavitation development for 3%  $\psi^+$  drop and 3%  $\chi^+$  drop, respectively. For both inducers, tip cavitation seems similar in the situations in Figs. 12(a) and 12(b), whereas sheet cavities have increased significantly. In both situations, the size of the sheet cavities looks comparable in the two inducers. It implies that the distance on each blade between the cavity downstream end and the cascade throat is different in the two inducers. For 3%  $\chi^+$  drop, the sheet cavities have nearly reached the throat in IND5, while they are much shorter than the cascade throat in IND3. It suggests that the inception of the  $\chi^+$

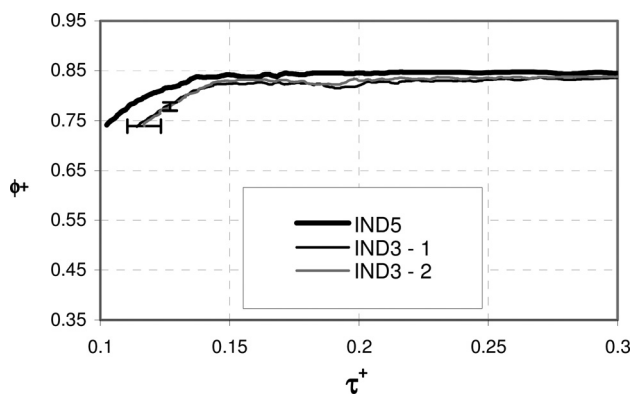


Fig. 10 Flow rate coefficient drop for IND3 and IND5 ( $N_{ref}$ ,  $Q_n$ , type #2 experiments)

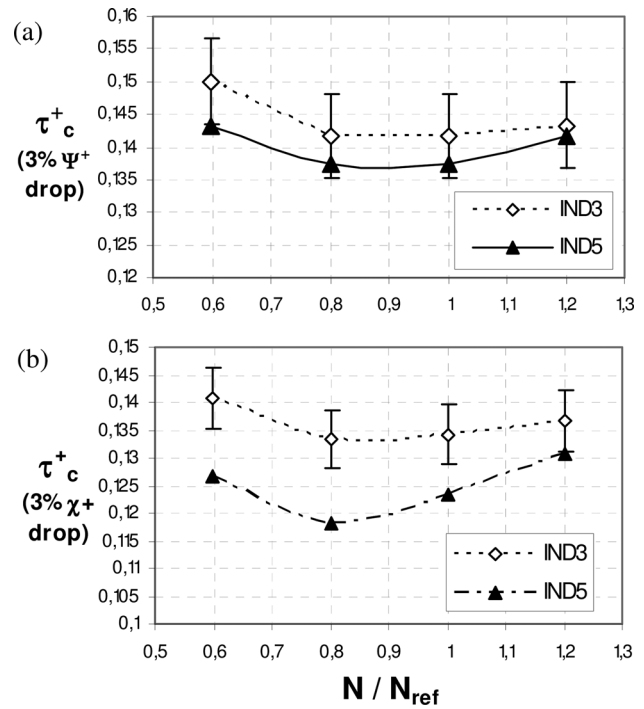


Fig. 11 Influence of the rotation speed on the value of  $\tau_c$  corresponding to (a) 3%  $\psi^+$  drop and (b) 3%  $\chi^+$  drop ( $Q_n$ , type #2 experiments)

breakdown is not directly connected to the extension of the sheet cavities into the blade to blade channels.

Figures 11(a) and 11(b) confirm the tendency observed in Figs. 8 and 9; when the pressure is decreased, the  $\psi^+$  and  $\chi^+$  drops both occur first in IND3 then in IND5. This classification does not depend on the rotation speed. As well for the 3%  $\psi^+$  drop as for the 3%  $\chi^+$  drop, the evolution of  $\tau_c^+$  with the rotation speed is small between  $0.6 N_{ref}$  and  $1.2 N_{ref}$  regarding the measurement uncertainties indicated on the charts. It confirms that the breakdown mechanism complies with the similarity laws, in the range of rotation speeds that was investigated here.

Influence of the mass flow rate on the breakdown is also investigated in Figs. 13 and 14. All results are obtained at rotation speed  $N_{ref}$  from type #2 experiments.

Concerning the 3%, 10%, and 20%  $\psi^+$  drop charts (Fig. 13), a quite stable value of  $\tau_c^+$  according to the mass flow rate is obtained for IND5. The maximum difference with the value at nominal flow rate is about 10%. Conversely, charts obtained with IND3 exhibit for  $Q/Q_n < 1$  a significant increase of  $\tau_c^+$  obtained at 3%  $\psi^+$  drop and a decrease of  $\tau_c^+$  obtained at 10% and 20%  $\psi^+$  drop. This indicates that the head drop is very progressive in such conditions. Such behavior may be related to an increase of the head losses in the stator downstream from the inducer, rather than to a decrease of the inducer performance.

The  $\chi^+$  drop charts (Fig. 14) confirm this point. The value of  $\tau_c^+$  obtained for 3%  $\chi^+$  drop remains nearly constant for all mass flow rates, which shows that the inducer performance is not reduced at the inception of the  $\psi^+$  drop. It can be also remarked that the 10%  $\chi^+$  and  $\psi^+$  drop charts have similar evolutions for both inducers. This suggests that the final breakdown sequence is directly linked to the inducer performance reduction due to the increase of cavitation.

Figure 14 shows that the inception of the  $\chi^+$  drop occurs sooner at partial flow rate for IND5. It may be related to the increase of the flow incidence at the blade leading edge, which results in a higher local blade load and thus in larger sheet cavities. IND3 behaves differently.  $\tau_c^+$  obtained for 3%  $\chi^+$  drop does not increase for small mass flow rates. However, IND3 is characterized by a high blade

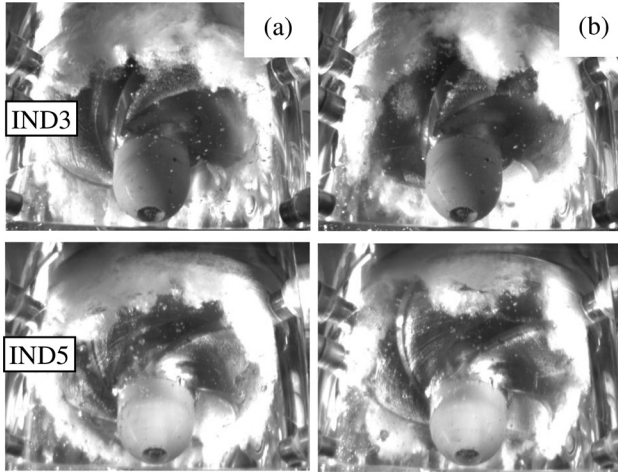


Fig. 12 Flow visualizations for (a) 3%  $\psi^+$  drop and (b) 3%  $\chi^+$  drop ( $0.6 N_{ref}, Q_n$ )

load even at nominal flow rate, so the increase of incidence at small flow rate may have less consequence than for the other inducer.

From the results presented in Figs. 8–14, it can be concluded that IND3 has the less interesting behavior regarding the breakdown. As a matter of fact, for nearly all flow rates and all rotation

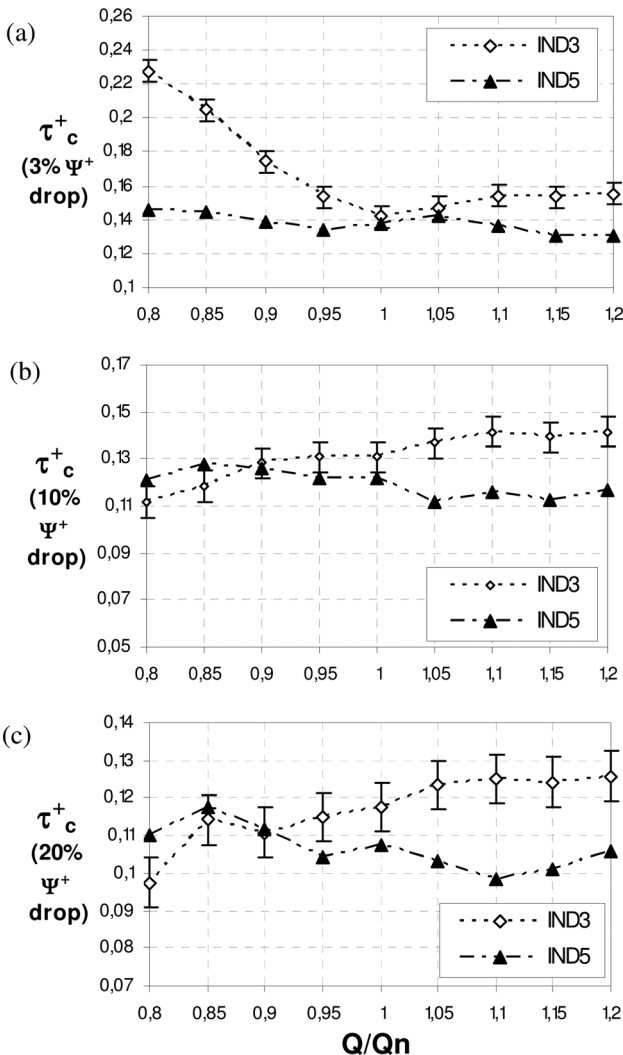


Fig. 13 Evolution of  $\tau_c^+$  according to the mass flow rate for (a) 3%, (b) 10%, and (c) 20%  $\psi^+$  drop

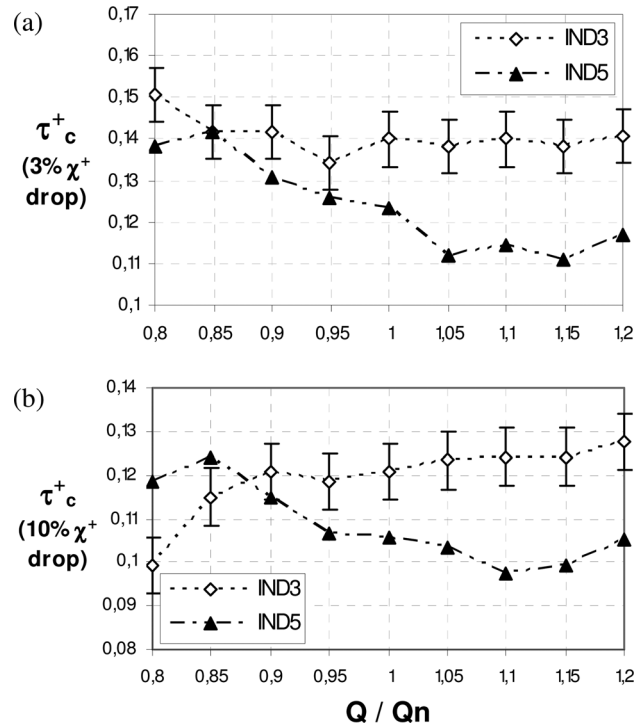


Fig. 14 Evolution of  $\tau_c^+$  according to the mass flow rate for (a) 3% and (b) 10%  $\chi^+$  drop

speeds, the  $\psi^+$  and/or  $\chi^+$  drop occurs first with IND3 then with IND5. Poor results obtained with IND3 may be related to the high blade load due to the small number of blades, which results in higher pressure difference between both sides of the blades and, thus, in larger sheet cavities on the suction side. This point is confirmed by visualizations of the sheet cavity evolution for  $\tau^+$  varying from 0.2 (before onset of performance breakdown) down to 0.1 (end of the experiment). It is clear that for such values of  $\tau^+$ , sheet cavities are much larger in IND3 than IND5, which was not the case at higher value of  $\tau^+$  (see Fig. 7 for  $\tau^+ = 0.25$ ). This may be a consequence of the design process, which results in nearly identical blade angles at the leading edge in both inducers, while the bending of the blades downstream is of course different because the loads are different. So, moderate cavitation conditions lead to identical short cavities, while decreasing  $\tau^+$  induces sheet cavities much larger in IND3 than in IND5.

#### 4 Investigation of the Flow Instabilities

From the six-component balance measurements performed during type #2 experiments, the evolution of the radial forces is investigated in the present section. The time-averaged magnitude of the forces is first considered. Then, the discussion focuses on the flow instabilities that can be detected from the frequency analysis of the signals.

**4.1 Mean Radial Forces.** The two components  $F_y$  and  $F_z$  of the radial force follow very similar evolutions, so attention is focused hereafter on  $F_y$  only. The mean and RMS values are obtained from a sliding treatment of the signal based on a 2 s window (4096 samples) with overlapping 62.5% (2560 samples). The evolution of the mean and RMS values during the pressure decrease are discussed hereafter. No figure is given for reasons of confidentiality. It is found that the mean radial force increases systematically between  $\tau^+ = 0.2$  and the breakdown while the RMS fluctuations become significant for  $\tau^+$  lower than 0.5. It suggests that pronounced unbalanced flow patterns occur mainly for  $\tau^+$  lower than 0.2 while fluctuations related to other types of flow

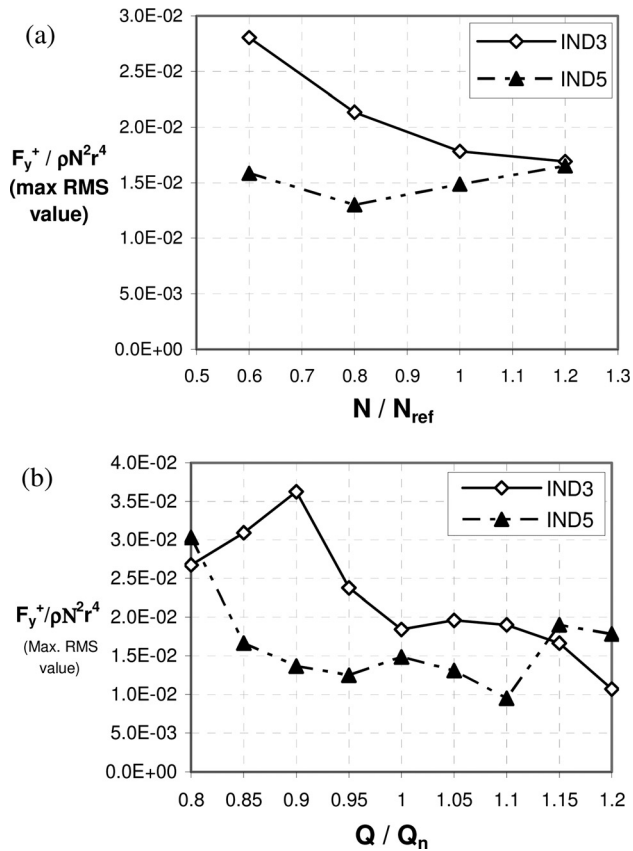


Fig. 15 Influence of (a) the rotation speed and (b) the mass flow rate on the maximum value of the RMS fluctuation of  $F_y^+$  (type #2 experiment)

instabilities occur for higher values of  $\tau^+$ , i.e., for moderate cavitation development in the inducers.

The increase of the RMS fluctuations occurs for  $\tau^+$  close to 0.45 for both inducers, which corresponds almost to the inception of the sheet cavities on the blades. It implies that radial force fluctuations are mainly related to sheet cavities. Conversely, tip cavitation, which is as much developed as well in IND3 as in IND5, seems to be not involved in the fluctuations since their amplitude is very different in IND3 and IND5.

As a matter of fact, significant differences between the inducers are obtained regarding the RMS fluctuations of  $F_y^+$ . IND3 is characterized by strong fluctuations for  $0.2 < \tau^+ < 0.4$  and during the final breakdown. For intermediate values of  $\tau^+$ , the amount of the fluctuations is small. The same qualitative behavior is obtained with IND5, but the amplitude of the fluctuations is much lower than with IND3.

Figure 15 presents the evolution of the maximum RMS value of  $F_y^+$  obtained during the whole duration of the experiment according to the rotation speed and the mass flow rate, respectively.

Dimensionless values of  $F_y^+$  are drawn to estimate whether the charts follow similarity laws or not. As a matter of facts, charts for IND5 are reasonably close to similarity laws, whereas a significant decrease of  $F_y^+ / N^2$  with  $N$  is obtained for IND3. However, highest values of  $F_y^+$  fluctuations correspond, according to the inducer, to different parts of the charts and, thus, to different phenomena: moderate cavitating conditions for IND3 and performance breakdown for IND5.

Figure 15 shows that the magnitude of the maximum RMS fluctuations of  $F_y^+$  depends strongly on the mass flow rate. The analysis at all investigated flow rates of the RMS fluctuations of the radial forces enables us to assess that the magnitudes obtained over  $Q_n$  are due to the same phenomena as the ones identified previously at  $Q_n$  for IND3 and IND5, whereas at partial flow rate,

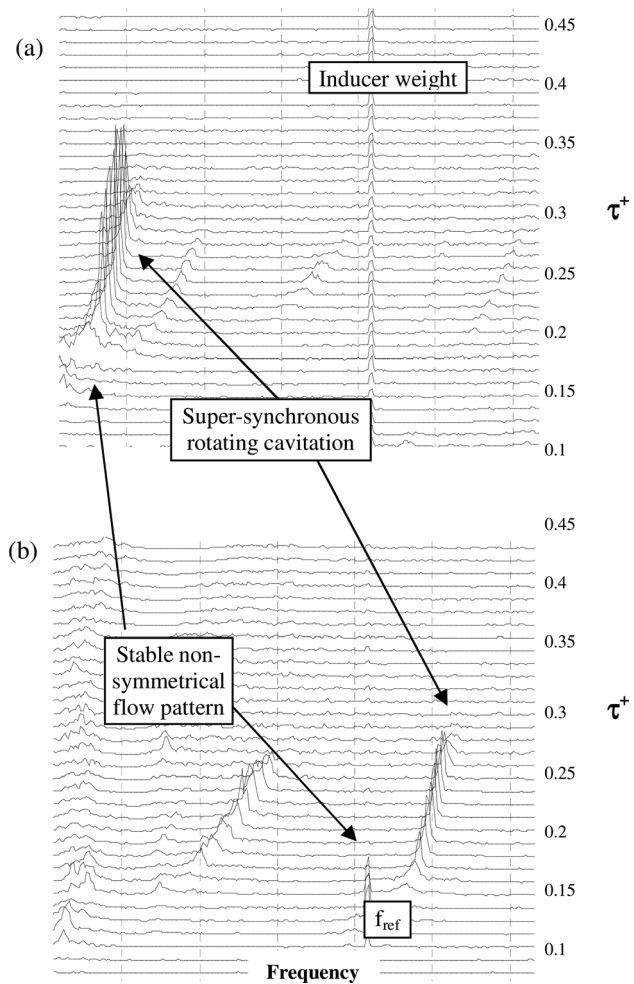


Fig. 16 Spectral analysis of (a)  $F_y$  and (b)  $P_2'$  (IND3,  $Q_n$ ,  $N_{ref}$ )

maximum amplitudes are systematically obtained during the breakdown:

- In the case of IND3, the magnitude of the fluctuations obtained for  $0.2 < \tau^+ < 0.4$  remains nearly constant at all mass flow rates, while the amplitude of the fluctuations during the breakdown increases when the mass flow rate decreases and becomes preponderant for  $Q/Q_n < 0.95$ .
- In the case of IND5, only the fluctuations that occur during the performance breakdown are of significant amplitude for all mass flow rates.

**4.2 Cavitation Instabilities.** Cavitation instabilities have been detected by frequency analysis of the measurement performed with the six-component balance. A FFT is applied to each bloc derived from the sliding treatment of the signals. Attention is focused on the radial forces  $F_y$  and  $F_z$ , whose analysis enables us to detect nonsymmetrical flow patterns that characterize the flow instabilities. Precision of the FFT is 0.5 Hz. An identical treatment is also applied to the signals of the fluctuating pressures  $P_1'$  and  $P_2'$  in order to detect rotating flow patterns in the stationary frame.

Figure 16 presents an example of result in the case of IND3 at nominal flow rate and reference rotation speed. For such flow conditions, super-synchronous rotating cavitation is clearly detected for  $0.18 < \tau^+ < 0.3$ . It is identified by the low frequency that is obtained in the rotating frame from the  $F_y$  signal, which is correlated with the peaks that can be seen from the analysis of  $P_2'$ , at frequency  $f_{RC}$  higher than the one of the inducer rotation. This pattern basically consists of large scale fluctuations of the radial force components  $F_y$  and  $F_z$  (Fig. 17) at a frequency that progressively decreases from a few tens of Hertz down to zero. A 90 deg

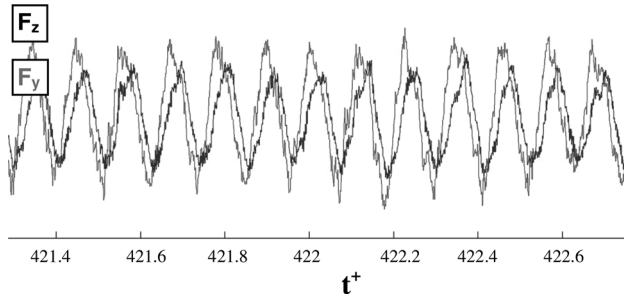


Fig. 17  $F_y$  and  $F_z$  fluctuations during the super-synchronous rotating cavitation (IND3,  $N_{ref}$ ,  $Q_n$ ,  $\tau^+ \approx 0.25$ , low-pass filter with cutoff frequency 400 Hz)

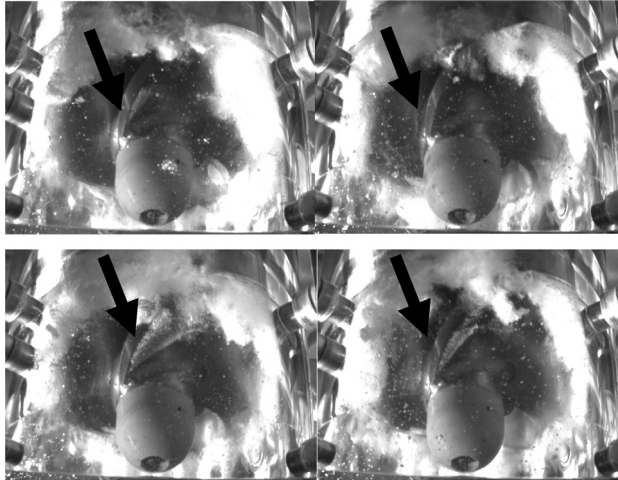


Fig. 18 Front views of the inducer during super-synchronous rotating cavitation (IND3,  $0.6 N_{ref}$ ,  $Q_n$ )

phase difference between  $F_y$  and  $F_z$  is observed, which suggests that these fluctuations may be associated to a rotating instability.

Visualizations performed at  $0.6 N_{ref}$  during type #2 experiments clearly show sheets cavities of variable size (Fig. 18). On the blade located at the top of the pictures, for example, large fluctua-

tions of the sheet cavity length are observed on the four proposed examples, which corroborates the hypothesis of rotating instability.

This assumption is confirmed by the analysis of the pressure signal (Fig. 19). Indeed, periodical fluctuations at frequency  $f_{ref} + 20\%$  decreasing down to  $f_{ref} + 10\%$  are obtained with a 90 deg phase difference between  $P'_1$  and  $P'_2$ . This is the evidence of a super-synchronous rotating two-phase flow situation.

It can be noticed in Fig. 16 that a second spectral line, at lower frequency is also obtained during the super-synchronous regime in the FFT of the pressure signals. This spectral line is detected for  $0.22 < \tau^+ < 0.29$  only, so it is not fully correlated with super-synchronous cavitation. It may thus correspond to a supplementary phenomenon, which may be disconnected from rotating cavitation. It is quite complicated to identify this low frequency on the time pressure signals because it is on the same order of magnitude as  $f_{RC}$ , so it mainly results in a modulation of the amplitude of the primary fluctuations at frequency  $f_{RC}$ . However, this secondary frequency can be observed in Fig. 19, with no phase difference between  $P'_1$  and  $P'_2$ . This suggests that it may be related to a global pulsation of the cavitation inside the inducer, such as self-oscillations of sheet cavities on the blades. This type of instability is not systematically forced by a pressure or mass flow rate fluctuation. It may also appear naturally for particular size of the sheet cavities. It is associated with periodical reentrant jet, whose mechanisms have been exhaustively analyzed in simplified 2D flow situations [13–16].

For lower cavitation number ( $0.16 < \tau^+ < 0.19$ ), a stable non-symmetrical flow pattern is detected. It is characterized by different but nearly constant levels of  $F_y$  and  $F_z$ , related to a steady radial load in the rotating frame (Fig. 20). It can be also identified on the pressure signals by periodical fluctuations at the inducer rotation frequency  $f_{ref}$  (rotation frequency of the load in the steady frame) with a 90 deg phase difference between  $P'_1$  and  $P'_2$  (Fig. 21). It can be postulated that this radial load is due to a nonperiodical distribution of the cavitation areas in the three blade to blade channels, but the present visualizations do not enable us to determine whether the attached sheet cavities or tip cavitation areas are affected.

Figure 22 presents the various flow instabilities that are detected from the FFT analysis of the force and pressure signals for a mass flow rate varying between 0.8 and  $1.2 Q_n$  and for  $\tau^+$  decreasing from low cavitating conditions down to the performance breakdown. Both inducers are considered here. Some of the frequency

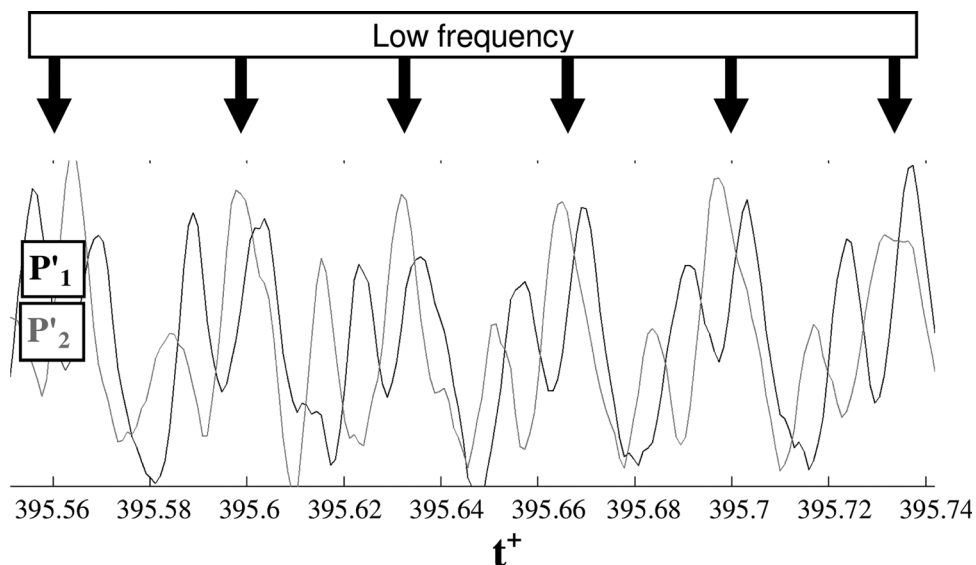


Fig. 19  $P'_1$  and  $P'_2$  fluctuations during the super-synchronous rotating cavitation (IND3,  $N_{ref}$ ,  $Q_n$ ,  $\tau^+ \approx 0.25$ , low-pass filter with cutoff frequency 200 Hz)

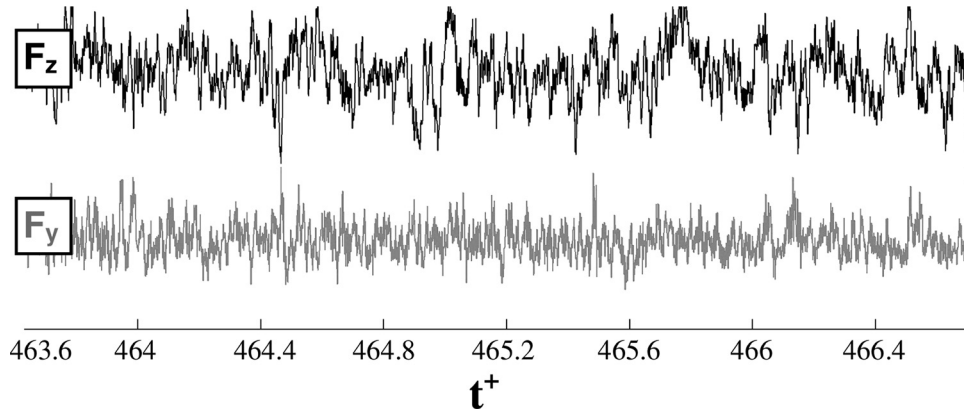


Fig. 20  $F_y$  and  $F_z$  fluctuations during the stable nonsymmetrical regime (IND3,  $N_{ref}$ ,  $Q_n$ ,  $\tau^+ \approx 0.17$ , low-pass filter with cutoff frequency 400 Hz)

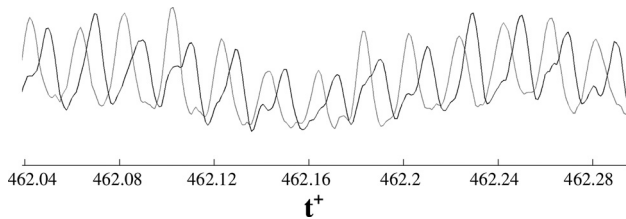


Fig. 21  $P_1$  and  $P_2$  fluctuations during the stable nonsymmetrical regime (IND3,  $N_{ref}$ ,  $Q_n$ ,  $\tau^+ \approx 0.17$ , low-pass filter with cutoff frequency 200 Hz)

peaks can be clearly related to a physical phenomenon, as in the two previous examples, while in other cases, interpretation is not so clear.

As can be seen from the results, rotating cavitation is obtained in both inducers for mass flow rates equal or superior to the nominal one. Note that in IND5, only subsynchronous cavitation has been clearly identified. In addition, another regime characterized by a low frequency in the rotating frame may be related to super-synchronous cavitation, but the evidence of this could not be obtained here. Stable nonsymmetrical flow patterns are also observed in both cases still above the nominal mass flow rate. Several other frequency peaks are also reported in Fig. 22 (during the breakdown for IND5 at partial flow rate and/or high cavitation number for IND3), but the understanding of the physical phenomena associated to them would require further measurements.

Some of these results are consistent with the numerical study reported previously by Horiguchi et al. [17], which was devoted to the investigation of the effect of the blade number on stable and unstable modes of cavitation in impeller cascades. From a linear stability analysis, the authors concluded that symmetrical cavitation patterns were preponderant in three blades and five blades impellers, while other steady configurations such as alternate cavitation or asymmetric cavitation was not found. This is almost the case here for IND5, and nonsymmetrical stable cavitation is obtained in IND3 only for a narrow range of  $\tau^+$ . Rotating cavitation is reported for all cascades, which is consistent with the present results. However, quantitative comparisons of instability frequency in the two studies cannot be performed because of the particular geometry of impeller cascade that was considered by Horiguchi et al. [17].

Results presented in Fig. 22 globally show that the two considered inducers are characterized by different “signatures” in the frequency domain. Moreover, the understanding of the flow organization associated with each frequency peak is not straightforward. Even classical behaviors of rotating cavitation, which have been already studied in four-blade inducers (see Coutier-Delgosha et al. [6]), seem related to complex unsteady behaviors, as in the

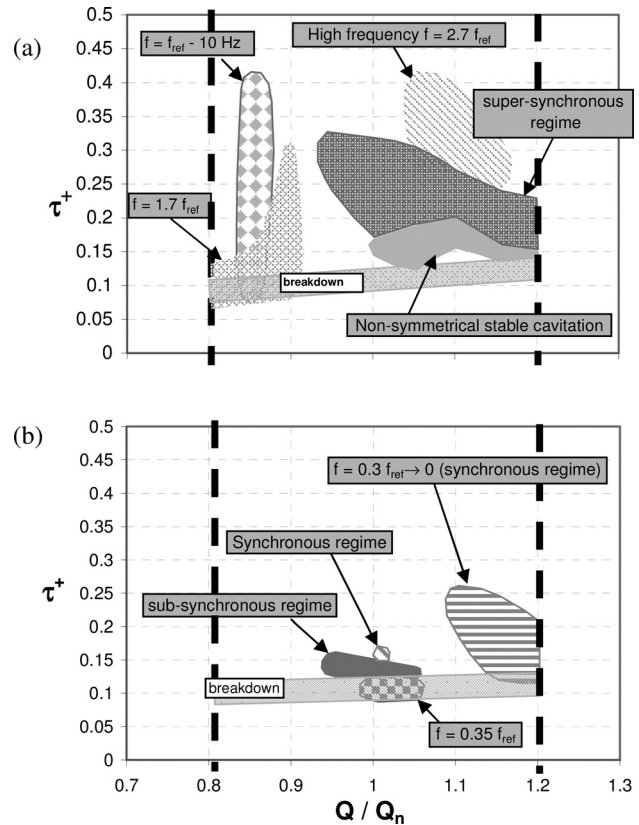


Fig. 22 Cartography of the frequencies detected for (a) IND3 and (b) IND5. Indicated frequencies are related to the rotating frame.

example presented previously for IND3. Therefore, a more in-depth analysis of the signals is necessary to make clearer the physical mechanisms involved in the detected nonsymmetrical flow patterns.

## 5 Conclusion

The comparison between three blade and five blade inducers has been performed in this study on the basis of mean flow characteristics and high frequency signals provided by the six-components balance mounted on the inducer shaft. The organization of cavitation in the inducers, the performance breakdown, and the fluctuations of the radial force have been investigated for rotation speeds varying between  $0.6 N_{ref}$  and  $N_{ref}$ , and mass flow

rates in the range  $0.8 Q_n$  to  $1.2 Q_n$ . Significant differences but also some resemblances between the two inducers have been found:

- IND3 and IND5 are both characterized by large scale tip cavitation, while previous visualization performed in four-blade inducers mainly show sheet cavitation.
- When the pressure is decreased, the performance breakdown occurs first with IND3, then with IND5. Rotation speed has only a little influence on this phenomenon, whereas mass flow rate variations have significant effects on the inception of the breakdown.
- Fluctuations of the radial force components are due to different phenomena in the two inducers for  $Q/Q_n > 1$ . Conversely, at partial flow rate they are systematically due to the instabilities that occur during the breakdown.
- Frequency analysis of the force and pressure high frequency signals have revealed for both inducers situations of rotating cavitation that require further investigation to complete their understanding.

### Acknowledgment

The present study was performed in the frame of contractual activity with SNECMA Moteurs and the CNES (French Space Agency).

The technical staff of the LML laboratory was much involved in the development and the operation of the test facility. The authors wish to thank especially J. Choquet and P. Olivier for their collaboration.

### Nomenclature

$A_a$  = casing vibration in the axial direction ( $m/s^2$ )  
 $A_r$  = casing vibration in the radial direction ( $m/s^2$ )  
 $F_x$  = axial component of the force on the shaft (N)  
 $F_y, F_z$  = radial components of the force on the shaft (N)  
 $\dot{N}$  = rotation speed ( $s^{-1}$ )  
 $N_{ref}$  = reference rotation speed ( $s^{-1}$ )  
 $\Delta P$  = pressure elevation  $P_d - P_i$  (Pa)  
 $P_i$  = absolute pressure in the inlet pipe (Pa)  
 $P_d$  = absolute pressure in the delivery pipe (Pa)  
 $P_{t_i}$  = total absolute pressure in the inlet pipe (Pa)  
 $P_{t_d}$  = total absolute pressure in the delivery pipe (Pa)  
 $P_{vap}$  = vapor pressure (Pa)  
 $P'_1, P'_2$  = fluctuating pressures at the inducer inlet (Pa)  
 $P'_3$  = fluctuating pressure at the inducer outlet (Pa)  
 $M_x$  = torque on the inducer shaft (Nm)  
 $M_{y,z}$  = bending moments on the shaft (Nm)  
 $Q$  = volumic flow rate ( $m^3/s$ )  
 $Q_n$  = nominal flow rate ( $m^3/s$ )

$Q_m$  = main flow rate (in the delivery pipe) ( $m^3/s$ )  
 $Q_s$  = secondary flow rate (for axial equilibrium) ( $m^3/s$ )  
 $r$  = inducer tip radius (m)  
 $t$  = time (s)  
 $\nu$  = outlet ratio hub radius/tip radius  
 $\Psi$  = head coefficient  $(P_{t_d} - P_{t_i})/(\rho \omega^2 r^2)$   
 $\chi$  = torque coefficient  $M_x/(\rho \omega^2 r^5)$   
 $\varphi$  = flow rate coefficient  $Q/(\pi \omega r^3 (1 - \nu^2))$   
 $\tau$  = cavitation number  $(P_{t_i} - P_{vap})/(\rho \omega^2 r^2)$

### References

- [1] Kubota, A., Kato, H., Yamaguchi, H., and Maeda, M., 1989, "Unsteady Structure Measurement of Cloud Cavitation on a Foil Section Using Conditional Sampling Technique," *ASME J. Fluids Eng.*, **111**, pp. 204–210.
- [2] Le, Q., Franc, J. P., and Michel, J. M., 1993, "Partial Cavities: Global Behavior and Mean Pressure Distribution," *ASME J. Fluids Eng.*, **115**, pp. 243–248.
- [3] Jousselein, F., De Bernardi, J., Goirand, B., and Delannoy, Y., 1992, "Analyse par films ultrarapides de poches de cavitation sur l'Inducteur de la Turbopompe à Hydrogène d'un Moteur Fusée," 5<sup>ème</sup> colloque de visualisation et de traitement d'images en Mécanique des Fluides, Poitiers.
- [4] Kamijo, K., Shimura, T., and Watanabe, M., 1977, "An Experimental Investigation of Cavitating Inducer Instability," ASME Paper No. 77-WA/FW-14.
- [5] Tsujimoto, Y., Kamijo, K., and Yoshida, Y., 1993, "A Theoretical Analysis of Rotating Cavitation in Inducers," *ASME J. Fluids Eng.*, **115**, pp. 135–141.
- [6] Coutier-Delgosha, O., Courtot, Y., Jousselein, F., and Reboud, J. L., 2004, "Numerical Simulation of the Unsteady Cavitation Behavior of an Inducer Blade Cascade," *AIAA J.*, **42**(3), pp. 560–569.
- [7] Yoshida, Y., Sasao, Y., Okita, K., Hasegawa, S., Shimagaki, M., and Ikohagi, T., 2007, "Influence of Thermodynamic Effect on Synchronous Rotating Cavitation," *ASME J. Fluids Eng.*, **129**, pp. 871–876.
- [8] Bakir, F., Kouidri, S., Noguera, R., and Rey, R., 2003, "Experimental Analysis of an Axial Inducer Influence of the Shape of the Blade Leading Edge on the Performances in Cavitating Regime," *ASME J. Fluids Eng.*, **125**, pp. 293–301.
- [9] Yoshida, Y., Tsujimoto, Y., Kataoka, D., Horiguchi, H., and Wahl, F., 2001, "Effects of Alternate Leading Edge Cutback on Unsteady Cavitation in 4-Bladed Inducers," *ASME J. Fluids Eng.*, **123**, pp. 762–770.
- [10] Horiguchi, H., Takashina, T., and Tsujimoto, Y., 2006, "Theoretical Analysis of Cavitation in Inducers With Unequally Spaced Blades," *JSM Int. J., Ser. B*, **49**(2), pp. 473–481.
- [11] Japikse, D., 2001, "Overview of Industrial and Rocket Turbopump Inducer Design," Proceedings of the 4th International Symposium on Cavitation, Pasadena, CA.
- [12] Coutier-Delgosha, O., 2001, "Etude des Ecoulements Cavitants: Modélisation des Comportements Instationnaires et Application Tridimensionnelle aux Turbomachines," Ph.D. thesis, INP Grenoble, Grenoble, France.
- [13] Furness, R. A., and Hutton, S. P., 1975, "Experimental and Theoretical Studies of Two-Dimensional Fixed-Type Cavities," *ASME J. Fluids Eng.*, **97**, pp. 515–521.
- [14] Stutz, B., and Reboud, J. L., 1997, "Experiments on Unsteady Cavitation," *Exp. Fluids*, **22**, pp. 191–198.
- [15] Stutz, B., and Reboud, J. L., 2000, "Measurements Within Unsteady Cavitation," *Exp. Fluids*, **29**, pp. 545–552.
- [16] Coutier-Delgosha, O., Stutz, B., Vabre, A., and Legoupil, S., 2007, "Analysis of the Cavitating Flow Structure by Experimental and Numerical Investigations," *J. Fluid Mech.*, **578**, pp. 171–222.
- [17] Horiguchi, H., Watanabe, S., and Tsujimoto, Y., 2000, "A Linear Stability Analysis of Cavitation in a Finite Blade Count Impeller," *ASME J. Fluids Eng.*, **122**(4), pp. 798–805.